TITLE:

Real-time Deterministic Prediction of Wave-induced Ship Responses Based on Short-time Measurements

AUTHOR(s):

Tomoki Takami[*1], Ulrik Dam Nielsen[*2,3], and Jørgen Juncher Jensen[*2]

*1 National Maritime Research Institute, Japan

*2 Technical University of Denmark, Denmark

*3 Centre of Autonomous Marine Operations and Systems, NTNU AMOS, Norway

E-mail: takami-t@m.mpat.go.jp

KEYWORDS:

Autocorrelation, Real-time Prediction, Nonstationary Wave-induced Response, Prolate Spheroidal Wave Functions,

ABSTRACT:

This paper studies real-time deterministic prediction of wave-induced ship motions using the autocorrelation functions (ACFs) from short-time measurements, namely the instantaneous ACFs. The Prolate Spheroidal Wave Functions (PSWF) are introduced to correct the large lag time errors in the instantaneous sample ACF, together with a modification of the autocorrelation (AC) matrix for ensuring its positive definiteness. The validity of the PSWF-based ACFs is first examined by using the ship motion measurements from model experiment under stationary wave excitations. It is shown that the use of PSWF-based ACFs leads to better prediction accuracy than direct use of sample ACFs. The validation is then extended to ship motion prediction using in-service data from a container ship, and an improvement of the prediction accuracy by PSWF-based ACFs is again found. Finally, the effectiveness of use of the instantaneous ACFs for non-stationary wave-induced responses is highlighted by comparing with the prediction results based on the ACFs from long-time measurements.

NOMENCLATURE

ACF	Autocorrelation Function
AC	Autocorrelation
PSWF	Prolate Spheroidal Wave Functions
AR	Auto-Regressive
SVM	Support Vector Machine
LSTM	Long-Short-Term-Memory
FFT	Fast Fourier Transform

PSD Power Spectrum Density
EVD Eigenvalue Decomposition
TEU Twenty-foot Equivalent Unit
LPF Low-pass Filter
CDF Cumulative Distribution Function
GPS Global Positioning System
JWA Japan Weather Association
NCEP National Centers for Environmental Predictions
NED North-East-Down

1. INTRODUCTION

Deterministic time domain prediction of wave-induced responses plays an important role for many types of marine operation. For instance, real-time prediction could benefit decision support systems related to, e.g., helicopter landings on the deck of a ship and crane and maintenance operations (on deep water) of offshore installations, but it may also be of direct use as input for motion stabilization systems with and without ship speed (Nakatani et al., 2006; Perez, 2005). Conventionally, AR models have been widely adopted for such prediction methods (Duan et al., 2015b). The AR models are useful methods in the sense that they do not require input about the waves. Recent researches have shown that the AR models are capable of predicting wave elevations and wave-induced responses (Duan et al., 2015a; Huang et al., 2015; Peña-Sanchez et al., 2020). However, it is critical that the model parameters need to be updated with off-line training thus not covering all operational scenarios, and moreover, the large number of training data prohibits real-time prediction because of too low computational efficiency (Huang et al., 2014). Meanwhile, recent machine learning techniques have matured and have been applied for achieving real-time prediction of waves and wave-induced responses. (Sclavounos and Ma, 2018) and (Ma et al., 2018) applied the SVM regression algorithm for wave elevation forecast. The LSTM deep learning model has been adopted to ship motion predictions most recently, see e.g. (Zhang et al., 2020). In this line, (Duan et al., 2019) demonstrated the effectiveness of LSTM on nonlinear ship motion. However, there are no consistent methods for assessing the length of time required for training even if such matured machine learning techniques are used, and this highlights the problems associated with the necessity for offline training and computational efficiency.

(Andersen et al., 2013) and (Nielsen et al., 2018; Nielsen and Jensen, 2017) assumed that the future wave-induced responses follow the expected mean variation of the conditional process, and then a different approach for deterministic response prediction using the measured ACF was investigated and demonstrated. In (Nielsen et al., 2018), the ACFs from long-time model-scale measurements via the FFT are utilized, and then reasonable prediction accuracy of ship motion under stationary sea states was demonstrated within 2-4 wave periods ahead, with real-time computations. However, the efficiency of this ACF-based method

using full-scale measurements is still open to doubt, as operation in real seaways (waves) are influenced by non-stationary conditions; not only may the seaway itself be non-stationary, but, maybe more importantly, the wave-induced responses should in many cases be considered as non-stationary because of effects related to maneuvering, e.g. changes in ship speed and heading relative to the waves within short time periods. Under these circumstances, the use of ACFs from long-time measurements for predictions will be questionable. In order to address such non-stationarities caused by both waves and maneuvering, it is ideal to make predictions using the ACFs from the shortest possible measurement period, namely 'instantaneous ACFs'.

When considering an application of the instantaneous ACFs to prediction, a concern about the large-lag time errors in the sample ACFs arises, as reported by, e.g., (Box et al., 2008). Thus, it is known that the sample ACF from time series measurements includes unphysical parts at large-lag time, since the practical measured signal is discretized and the measurement time window is limited (Box et al., 2008). This large-lag time error influences the prediction accuracy and smoothing of the ACF or the associated PSD is therefore necessary (Nielsen et al., 2018). Recently, the authors presented a new approach for obtaining smoothed ACF and PSD from short-time measurements (Takami et al., 2020b). In (Takami et al., 2020b), the PSWF (Slepian and Pollak, 1961) were used to taper the sample ACF for reducing the large-lag time errors. The tapered time length in ACF can be adjusted by changing the number of PSWF. The advantage of the PSWF-based approach is that one can adjust the tapered time length to any time, while maintaining high frequency resolution in PSD, unlike the FFT-based approach. Then, it is expected that the PSWF-based smoothing method will be useful for non-stationary wave-induced response predictions, as it allows for using only recent measurements with rather small computational efforts.

However, in (Takami et al., 2020b), a problem in making predictions using PSWF-based ACFs was found and discussed; a 'numerical concern' related to inversion of the AC matrix, which can become non-positive definite when the PSWF-based ACF is introduced. Although the sample AC matrix, per se, should be non-negative definite (McLeod and Jimenez, 1984), it is not necessarily the case for the PSWF-based AC matrices. This problem can be avoided to some degree by adding white noise to PSWF-based ACF as demonstrated in (Takami et al., 2020b), however, it is unclear what level of noise is appropriate. From this, the authors proposed the EVD based and PSD modification approaches towards the positive definite AC matrix (Takami et al., 2020c). By applying these approaches, a positive definiteness in AC matrices is secured. Moreover, it was shown that the PSD modification-based approach enables prediction in real-time, and the results of which are comparable to the computationally time-consuming EVD based approach.

In this paper, the effectiveness of the PSWF-based ACF together with AC matrix modification for deterministic prediction of the wave-induced ship motions is further investigated and demonstrated. To achieve the positive definiteness of the AC matrices assigning the PSWF-based ACFs, the PSD modification approach presented by (Takami et al., 2020c) is used. Experimental measurements of heave motion under a stationary sea state are first used for making a series of sensitivity analyses regarding

changeable parameters in the present PSWF-based prediction methods, while comparing the prediction accuracy with results from direct use of sample ACFs. Then, full-scale measurements from a large container ship in size of 14,000TEU (Okada et al., 2017) are used for validations. The ship motion time series under two different maneuvering conditions are used, and the validity of PSWF-based instantaneous ACF for predicting (non-stationary) ship motions is finally discussed.

2. ACF BASED PREDICTION BY PSWF

2.1. Conditional Prediction by ACF

The ACF-based conditional prediction adopted in this study is briefly introduced in this section. (Andersen et al., 2013; Lindgren, 1970; Nielsen et al., 2018; Nielsen and Jensen, 2017) can be referenced for the derivation of formulae and theoretical background.

Let t_0 be the start time of prediction. Using the recent n measurements, $x(t_0)$, $x(t_1)$,…, $x(t_{n-1})$ where $t_0>t_1>\ldots>t_{n-1}$, the predictions at time t ahead of current time (t_0) are given by

$$\hat{x}(t) = \mathbf{r}^T(t)\left(\mathbf{R}_n\right)^{-1}\mathbf{x} + x_{mean} \tag{1}$$

where x_{mean} denotes the mean value of $x(t_0)$, $x(t_1)$,…, $x(t_{n-1})$. $\boldsymbol{r}(t)$ denotes the autocorrelation vector, $\mathbf{R}_n$ the autocorrelation (AC) matrix, and $\mathbf{x}$ the measurement vector. Taking a constant time increment Δt:

$$\mathbf{r}(t) = \frac{1}{r(0)}\left[r(t-t_0) \quad r(t-t_0+\Delta t) \quad \cdots \quad r(t-t_0+(n-1)\Delta t)\right]^T$$

$$\mathbf{R}_n = \begin{bmatrix} 1 & \frac{r(\Delta t)}{r(0)} & \cdots & \frac{r((n-1)\Delta t)}{r(0)} \\ \frac{r(\Delta t)}{r(0)} & 1 & \cdots & \frac{r((n-2)\Delta t)}{r(0)} \\ \vdots & \vdots & \ddots & \vdots \\ \frac{r((n-1)\Delta t)}{r(0)} & \cdots & \frac{r(\Delta t)}{r(0)} & 1 \end{bmatrix} \tag{2}$$

$$\mathbf{x} = \left[x(t_0)-x_{mean}, x(t_1)-x_{mean}, \ldots x(t_{n-1})-x_{mean}\right]^T$$

where $r(t)$ denotes the ACF, which can be derived from either by using sample ACF directly or PSWF-based one based on the measurements prior to t_0.

2.2. Correction of Sample ACF by PSWF

If the sample ACF $r_s(t)$ is given by the time series measurements, then the PSWF-based ACF is written in the form (Takami et al., 2020b):

$$r_p(t) = \sum_{\substack{j=0 \\ j\ even}}^{N_e} a_j \psi_j(\frac{t}{T}, c), \quad 0 \le t \le T \tag{3}$$

where

$$a_j = 2\int_0^1 \psi_j\left(\frac{t}{T}, c\right) r_s\left(\frac{t}{T}\right) d\frac{t}{T} \tag{4}$$

Here ψ_j denotes the PSWF (Slepian and Pollak, 1961), c the Slepian frequency, N_e the number of PSWF components, and T the time length of ACF. If N_e takes a large value close to $2c/\pi$, r_p is very close to the sample ACF r_s within $0 \le t \le T$, while smaller N_e results in a smoothed ACF where r_p is converged to zero by a certain time (Takami et al., 2020b). Using the PSWF-based ACF r_p, the PSD is also explicitly expressed by PSWF, as

$$S_p(\omega) \approx \sum_{\substack{j=0 \\ j\ even}}^{N_e} a_j \frac{2}{\Omega\lambda_j} \psi_j(\frac{\omega}{\Omega}, c) \tag{5}$$

where λ_j denotes the scaled eigenvalues of PSWF, and Ω the upper limit of angular frequency which satisfies the following relationship (Slepian and Pollak, 1961)

$$c = T\Omega \tag{6}$$

The numerical derivation of PSWF is made using the Legendre polynomials-based approach presented by (Xiao et al., 2001). In this study, PSWF of c=300 and c=600 are adopted from here onwards. The absolute values of the scaled eigenvalues λ_j with respect to c=300 and c=600 are plotted in Fig. 1. Indeed, the largest $2c/\pi$ eigenvalues are dominant. The significant values of $|\lambda_j|$ become $|\lambda_j| \approx \sqrt{2\pi / c}$ (Moore and Cada, 2004). In many cases, $S_p(\omega)$ can be represented by using values of N_e smaller than $2c/\pi$ (Takami et al., 2020b). Since $|\lambda_j|$ are nearly constant when $N_e<2c/\pi$, see Fig. 1, the PSWF-based PSD $S_p(\omega)$ can be expressed by

$$S_p(\omega) \approx \sum_{\substack{j=0 \\ j\ even}}^{N_e} (-1)^{j-1} \frac{a_j}{\Omega} \sqrt{\frac{2c}{\pi}} \psi_j(\frac{\omega}{\Omega}, c) \tag{7}$$

without any needs of calculating λ_j. N_e can be determined by the time at which the PSWF-based ACF converges, as discussed in sub-section 3.3.2.

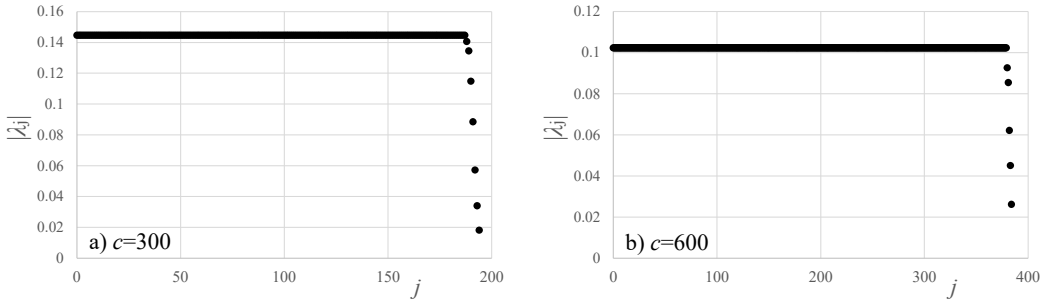

Fig. 1 Absolute values of the scaled eigenvalues λ_j with a) c=300 and b) c=600

2.3. Modification of AC Matrix by Removal of Negative PSD + White Noise

It is known that the eigenvalues of a Toeplitz matrix, like a typical AC matrix, are asymptotically correlated to the discretized PSD components, see e.g. (Gray, 2006). Indeed, it was shown in (Takami et al., 2020b) that the PSWF-based PSD by Eq. (5) may include negative PSD depending on N_e value. Thus, the removal of negative values in PSD may provide a way to modify the AC matrix ensuring the positive definiteness. The removal of negative values is made for a given threshold value of PSDs, which means that the modified PSD becomes

$$S_p^{*}(\omega_i) = S_p^{'}(\omega_i) + s$$
$$where \;\; S_p^{'}(\omega_i) = \begin{cases} \max\left\{S_p(\omega_i), 0\right\}; & 0 \le \omega_i \le \Omega \\ 0 \qquad\qquad\quad ; & \Omega \le \omega_i \le \omega_N \end{cases} \tag{8}$$

where s denotes the constant value (i.e. threshold) indicating a lower limit of PSD. Note that the upper limit of ω_i should be the Nyquist frequency, $\omega_N=\pi/\Delta t$., while the frequency range in PSWF-based PSD S_p defined by Eq. (5) is limited within $0\le\omega_i\le\Omega$. The modification by Eq. (8) implies that a bandlimited white noise is added to the nonnegative PSD $S_p'(\omega_i)$. When the white noise covers the frequency range $-\omega_N \le\omega_i\le \omega_N$, the ACF corresponding to constant value of s in PSD can be expressed in a form (Jensen, 2001)

$$r_n(t) = s\omega_N \frac{\sin(\omega_N t)}{\omega_N t} \tag{9}$$

Eq. (9) implies that the variance of white noise is equal to $s\omega_N$.

Here suppose that the noise level correlates to the negative area of PSD. Thus,

$$s = -\alpha \frac{\int_0^{\Omega} \min\left\{S_p(\omega_i), 0\right\} d\omega}{\omega_N} \tag{10}$$

where α denotes a correction factor to adjust the noise level, noting that α typically can be smaller than 1 as also discussed later. Then, the modified AC matrix becomes

$$\mathbf{R}_n^* = \frac{1}{r_p(0)} \begin{bmatrix} r_p^*(0) & r_p^*(\Delta t) & \cdots & r_p^*((n-1)\Delta t) \\ r_p^*(\Delta t) & r_p^*(0) & \cdots & r_p^*((n-2)\Delta t) \\ \vdots & \vdots & \ddots & \vdots \\ r_p^*((n-1)\Delta t) & \cdots & r_p^*(\Delta t) & r_p^*(0) \end{bmatrix} \tag{11}$$

where

$$r_p^*(t) = r_p'(t) + r_n(t) = \int_0^{\omega_N} S_p'(\omega) \cos(\omega t)\, d\omega + r_n(t) \tag{12}$$

according to the Wiener–Khinchin theorem. The inverse matrix of $\mathbf{R}_n^*$ can be assigned to Eq. (1) and be used for predictions. The corrected ACF $r^*(t)$ is also introduced into the autocorrelation vector as

$$\mathbf{r}^*(t) = \frac{1}{r_p(0)} \left[r_p^*(t - t_0) \quad r_p^*(t - t_0 + \Delta t) \quad \cdots \quad r_p^*(t - t_0 + (n-1)\Delta t) \right]^T \tag{13}$$

$\mathbf{r}^*(t)$ is then assigned to Eq. (1) and be used for predictions as well.

3. SENSITIVITY ANALYSIS BY USING EXPERIMENTAL MEASUREMENTS

3.1. Data Summary

In this section, the experimental measurements in (Nielsen et al., 2018) are used to validate the present ACF based prediction method using PSWF and to perform sensitivity analyses. The measurements originate from model tests with a platform supply vessel model in scale 1/30 with dimensions; L_{pp} = 1.97 [m] and B = 0.44 [m]. The model has eight 12 V batteries supplying power to the thrusters equipped in the model and a National Instruments™ CompactRIO (cRIO) that runs the dynamic positioned control system. The case of a heave motion time series of duration 780 [s] (named as '*Case* 2a' in (Nielsen et al., 2018)) is used, see

Fig. 2. The time series data have been measured at 20Hz, thus Δt=0.05 [s], under head sea condition with zero forward speed. A low-pass filter (LPF) with cut-off frequency of ω_{LPF}=20 [rad/s] is applied to exclude high-frequency noise, and a rectangular window is used as a window function. The stationary irregular waves are generated according to the JONSWAP type wave spectrum with significant wave height of 5.0 [cm] and peak wave period of 0.9 [s]. The PSD of heave motion is calculated by FFT and plotted in Fig. 3. The input wave spectrum is also plotted by a black dotted line, as a reference. The smoothing of the heave motion PSD is made by using WAFO (Brodtkorb et al., 2000) with smoothing window functions of 240 elements/weights as demonstrated in (Nielsen et al., 2018), and presented in Fig. 3 with a red solid line. The dominant frequency band of the heave motion is distributed widely within 5-10 [rad/s], as also observed in (Nielsen et al., 2018). Fig. 4 shows the CDF of the heave motion measurements, including the fitting by the normal distribution. Although an initial "run-in phase" may have appeared in the measured time series, the present heave motion can be regarded as a stationary process, since the CDF is very close to the normal distribution.

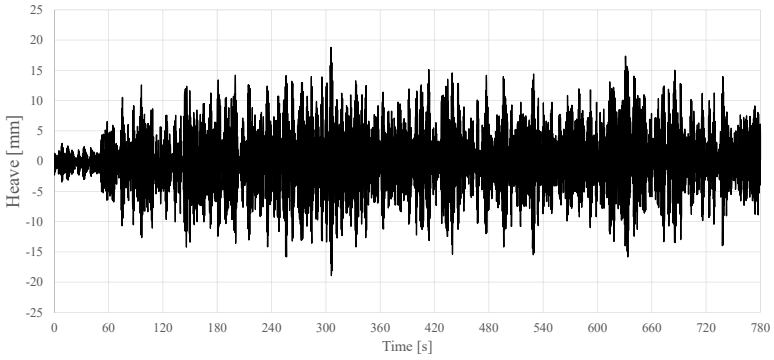

Fig. 2 Heave motion time series by experimental measurements (Nielsen et al., 2018)

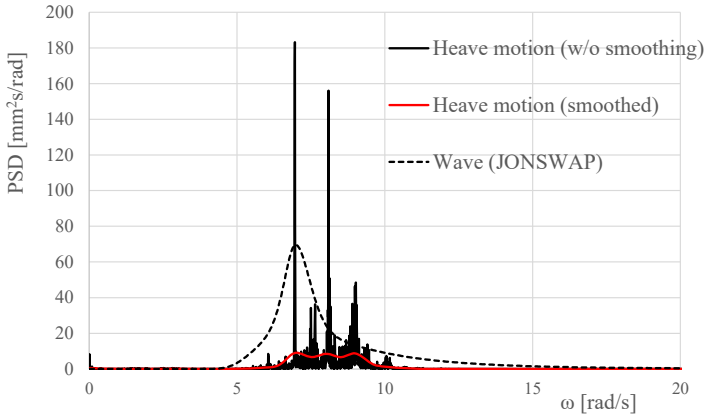

Fig. 3 PSD of heave motion time series and input wave spectrum

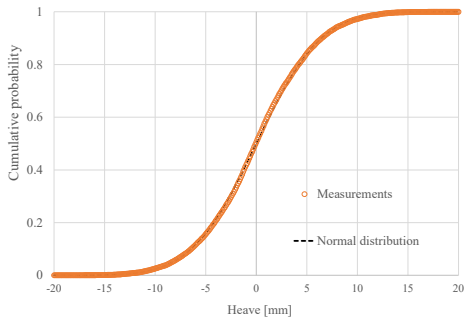

Fig. 4 Cumulative density function of heave motion from the model experiment

3.2. Prediction Setups

Three different combinations of *T* and Ω as listed in Table 1 are employed for a series of predictions by PSWF-based ACFs. The AC matrices of the size corresponding to the time length *T* are used for predictions, i.e. 201×201 on *Case* A and 301×301 on *Case* B and *Case* C. The instantaneous sample ACFs are calculated according to the following discretized form (Kitagawa, 2010),

$$r_{s,k} = \frac{1}{n} \sum_{m=k+1}^{n} (x_m - \mu_x)(x_{m-k} - \mu_x) \tag{14}$$

where μ_x denotes the mean value of discretized measurements x_m within $t_0 - T \le t \le t_0$ [s].

Note that for *Case* A and *Case* C, Ω values are larger than the cut-off frequency of the time signal, ω_{LPF}=20[rad/s]. In these cases, the PSWF-based PSD $S_p(\omega)$ occasionally includes non-zero value within $\omega_{LPF} \le \omega \le \Omega$ [rad/s] depending on the choice of N_e value. To avoid this, in *Case* A and *Case* C, $S_p{}'$ in Eq. (8) is redefined as

$$S_p{}'(\omega_i) = \begin{cases} \max\left\{S_p(\omega_i), 0\right\}; & 0 \le \omega_i \le \omega_{LPF} \\ 0 ; & \omega_{LPF} \le \omega_i \le \omega_N \end{cases} \tag{15}$$

The ACF-based predictions are made using the instantaneous ACFs from recent *T* [s] measurements in a sequential manner, introducing the updates of t_0. The prediction procedure is illustrated in Fig. 5. Initially, the start time of prediction t_0 is set as t_0=*T* and predictions are made up to t_{pre} [s] ahead. Then, the start time of prediction is updated to the end time of the prediction t_0+t_{pre} [s], and the next prediction is made to the next t_{pre} [s] ahead, until t_0+2t_{pre} [s]. This procedure is repeated up to 780[s]. Note that if sample ACFs are directly used for prediction, *Step* 2 and *Step* 3 are skipped. In this study, three different lengths of t_{pre} are

used, t_{pre}=1.5, 3.0, and 6.0 [s].

Table 1 Combinations of c, T, Ω, and AC matrix size for each case.

	c	T [s]	Ω [rad/s]	AC matrix size n
Case A	300	10	30.0	201
Case B	300	15	20.0	301
Case C	600	15	40.0	301

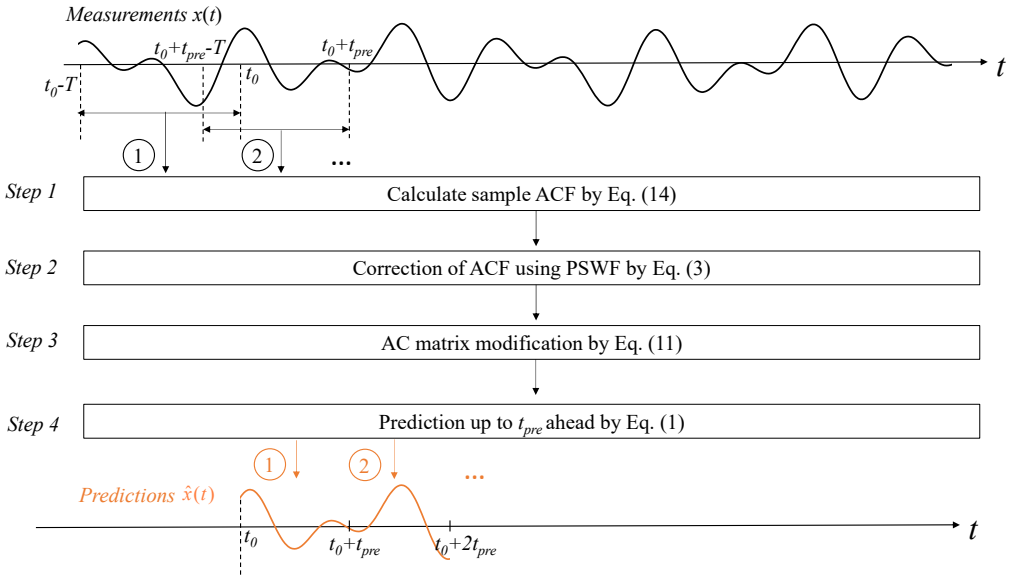

Fig. 5 Sequential prediction procedure using instantaneous ACFs

3.3. Validation and Sensitivity Analysis

3.3.1 ACF and PSD

First, a sample ACF (r_s) is calculated by 105-120 [s] measurements, and then PSWF-based ACFs given by Eq. (3) (r_p) and modified ones given by Eq. (12) (r_p^*) are compared. *Case* B is used for obtaining PSWF-based ACFs with the number of PSWFs is N_e=124. The noise correction factor α=1.0 and 0.1 are adopted to calculate the noise level given by Eq. (10). Derived ACFs are compared in Fig. 6. From the figure, the ACF is corrected by PSWF to converge to about 13 [s]. By applying the PSD modification, ACF value at t=0 [s] has slightly increased, while no significant change is found for t>0. Assuming that α=1.0, for instance, derived $s\omega_N$ is 4.3% of signal variance, which results in the small increase in the ACF around t=0 [s]. The PSDs from FFT of 105-120 [s] measurements, PSWF-based PSD given by Eq. (5) or Eq. (7) (S_p), and modified one given by Eq. (8) (S_p^*) are compared in Fig. 7. As noise levels $s\omega_N$ are only a few percent of the signal variances, the increment of PSD is not significant.

The PSWF-based ACF (r_p) and modified ACF (r_p^*) are introduced into the 301×301 AC matrices, and then the eigenvalues are examined. Fig. 8 shows a comparison of eigenvalues. Here, α=1.0 is employed. One can find that negative eigenvalues appeared without modification of ACF. By applying the present PSD modification approach, on the other hand, all the eigenvalues are indeed corrected to positive values. In contrast to the normal EVD based approach, e.g. see (McMurry and Politis, 2015), this PSD modification approach allows real-time computations.

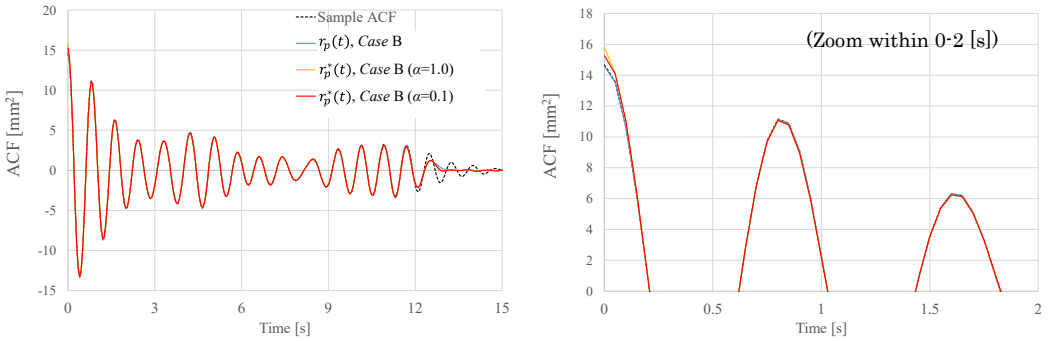

Fig. 6 Comparison of ACFs among sample ACFs, PSWF based ACF (r_p), and modified one (r_p^*). 105-120 [s] measurements are used for calculating sample ACF. N_e=124 is employed

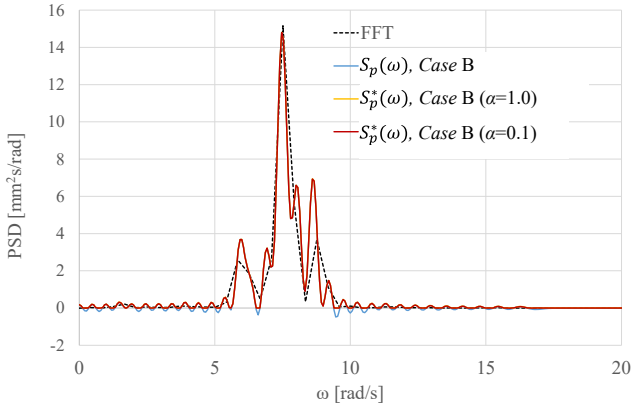

Fig. 7 Comparison of PSDs among FFT result, PSWF based ACFs (S_p), and modified one (S_p^*). 105-120 [s] measurements are used for calculating FFT. N_e=124 is employed

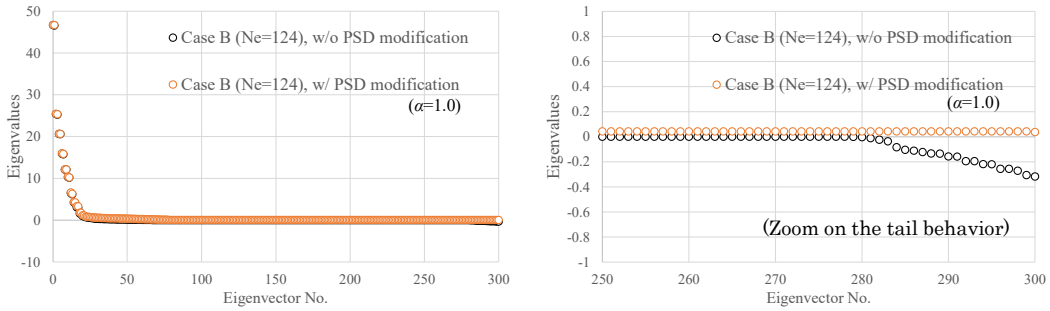

Fig. 8 Comparison of eigenvalues of 301×301 PSWF-based AC matrices with *Case* B, N_e=124

3.3.2 Smoothing of ACF by PSWF

It should be noted that when PSWF is used for expressing ACF, care should be taken not to choose too small number of PSWF N_e, while keeping the accurate expression of variance of the signal (Takami et al., 2020b). Using a sample ACF from the 105-120 [s] measurements, the non-dimensional variance values in PSWF-based ACFs for each case in Table 1, i.e. $r_p(0)/r_s(0)$, are calculated and plotted with respect to N_e values in Fig. 9. From Fig. 9, the accuracy of $r_p(0)$ value by PSWF has deteriorated for small N_e value cases, in particular when N_e<50 for *Cases* A and B and N_e<100 for *Case* C.

The convergence time of PSWF-based ACFs (hereafter, denoted as '*memory time*') are then examined. The memory time in ACFs is defined as the time over which the ACF converged to 0.1% of the signal variance or less, i.e. $0.001r_s(0)$, then the results are plotted with respect to N_e values in Fig. 10. Taking account of the lower limit of N_e values based on Fig. 9, one can make a choice of the convergence time of ACF between 6.2 and 10 [s] for *Case* A, and between 9 and 15 [s] for *Cases* B and C, respectively.

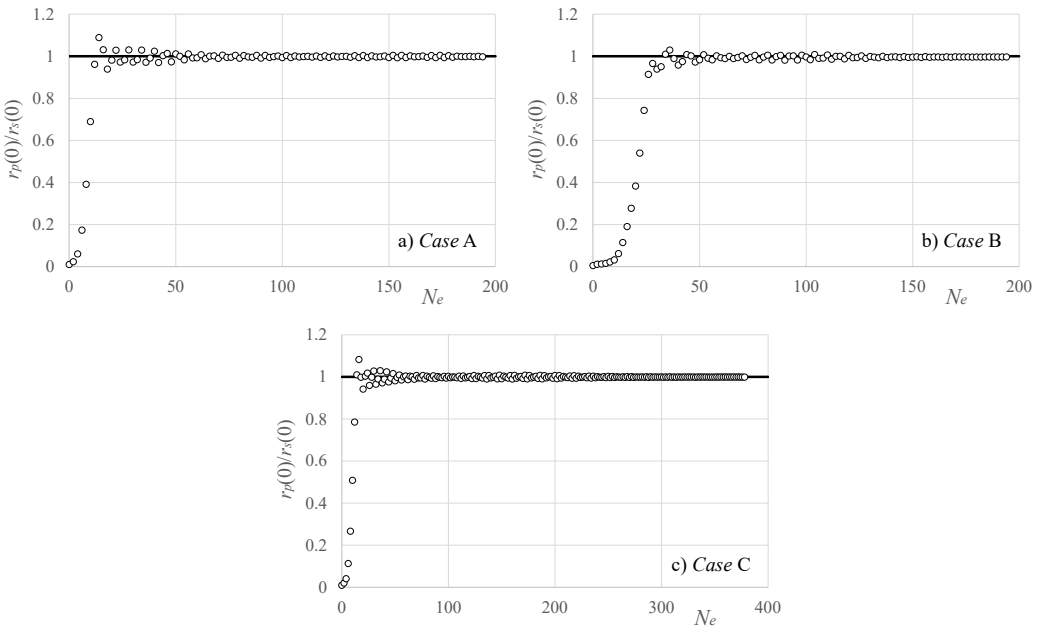

Fig. 9 Plots of $r_p(0)/r_s(0)$ with respect to N_e values

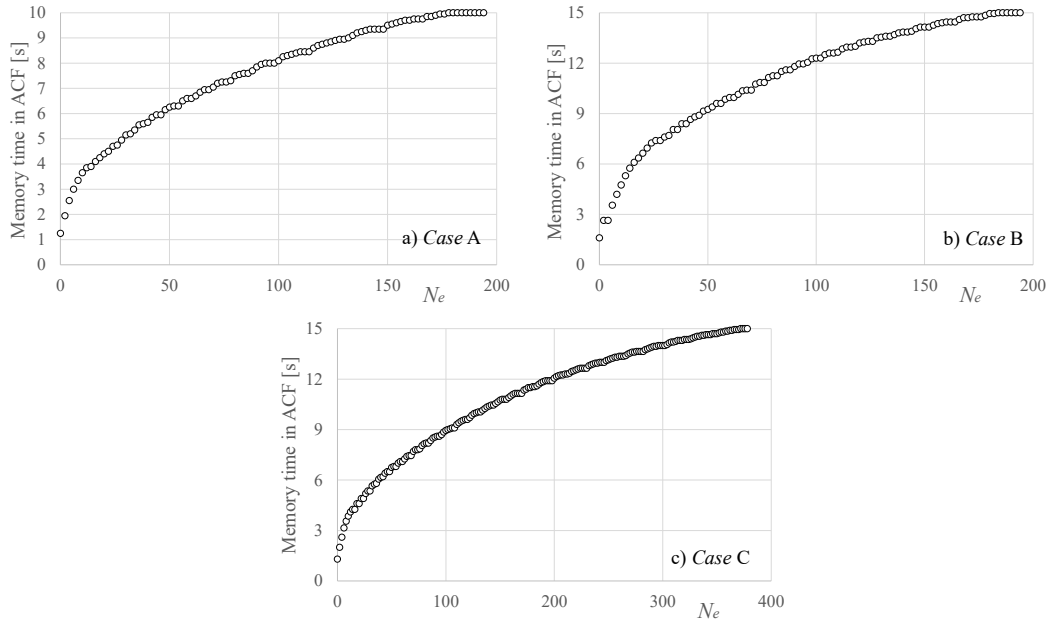

Fig. 10 Memory time of PSWF-based ACFs with respect to N_e values

3.3.3 Sensitivity analysis on noise level

Using the PSWF-based ACF along with AC matrix modification, a sensitivity analysis and validation of the prediction results are now made. First, a sensitivity analysis is devoted to investigating the effect of noise level. A series of predictions are made according to the procedure illustrated in Fig. 5 for each case, while changing α values in Eq. (10).

The prediction accuracy is evaluated by comparing with the measurements from a given time T [s] to 780 [s]. The Pearson Correlation Coefficient ρ is calculated in order to evaluate the prediction accuracy:

$$\rho = \frac{\sum_{i=1}^{N}(\hat{x}_i - \mu_{\hat{x}})(x_i - \mu_x)}{\sqrt{\sum_{i=1}^{N}(\hat{x}_i - \mu_{\hat{x}})^2}\sqrt{\sum_{i=1}^{N}(x_i - \mu_x)^2}} \tag{16}$$

where μ_x and $\mu_{\hat{x}}$ denote the mean values of measurements and predictions, respectively. N is the number of predictions or measurements corresponding to the time range from T [s] to 780 [s]. According to (Taylor, 1990), $\rho \leq 0.35$ is generally considered to reflect low or weak correlation, 0.36 to 0.67 modest or moderate correlation, while 0.68 to 1.0 indicates strong or high correlation. Another metric, like the Determination Coefficient R^2, may also give insights on prediction accuracies. However, in the following discussions focus will only be on ρ values, while results on R^2 are listed in Appendix 1 as supplemental information, since

checking ρ values should suffice to judge the prediction accuracy.

Under the prediction time length of t_{pre}=1.5 [s], the evaluated ρ are plotted with respect to α values for each case in Figs. 11, 12, and 13. N_e=124 is used on *Case* A and *Case* B, while N_e=250 is used on *Case* C. α values are changed within $0<\alpha<1$. In the figures, ρ from direct use of sample ACF are denoted by black dotted lines. From the figures, for *Case* A and *Case* C, the smaller α value apparently leads to better prediction accuracy rather than the direct use of sample ACF, as evaluated by ρ values. However, in the event of too small α value, e.g. in the case of α=0.0001, the accuracies are reduced. This is attributed to the near non-positive definiteness of AC matrices in some cases. As a reference, prediction results within 225-230 [s] from sample ACF, i.e. *Case* A with α=0.01 versus *Case* A with α=0.0001, are compared with the measurements in Fig. 14. The prediction results around 227-229 [s] show high frequency oscillations due to the near non-positive definiteness of AC matrices. Therefore, a selection of smallest possible α is ideal to obtain reliable prediction results by PSWF-based ACF. As for *Case* B results, the dependence on the noise level to the prediction accuracy is found to be more sensitive than the other cases. In this case, α=0.2 provides the best accuracy.

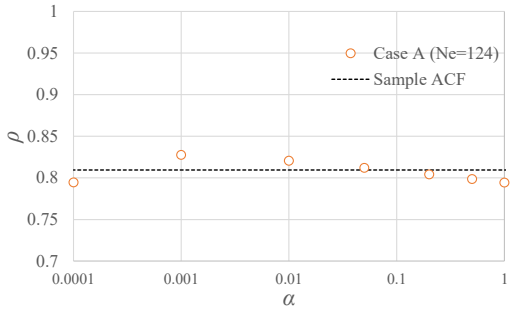

Fig. 11 Correlation coefficient ρ with respect to α values on *Case* A. N_e=124 and t_{pre}=1.5 [s] are applied

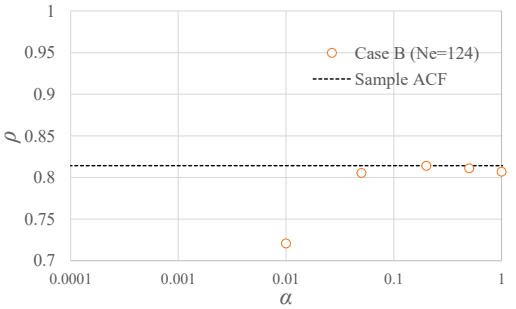

Fig. 12 Correlation coefficient ρ with respect to α values on *Case* B. N_e=124 and t_{pre}=1.5 [s] are applied

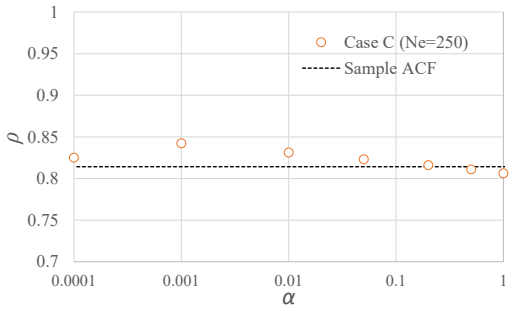

Fig. 13 Correlation coefficient ρ with respect to α values on *Case* C. N_e=250 and t_{pre}=1.5 [s] are applied

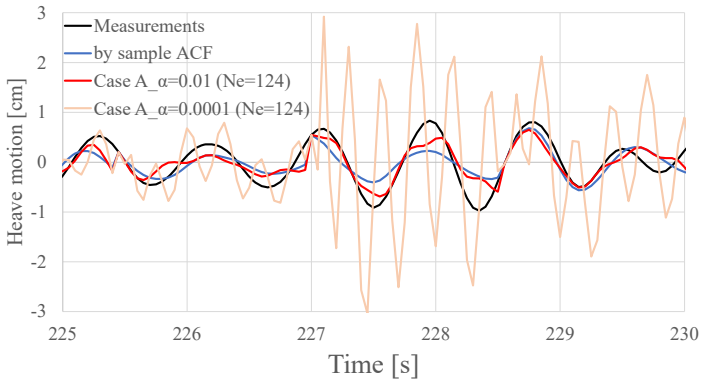

Fig. 14 Comparison of predictions results within 225-230 [s] by sample ACF and *Case* A with different α values. N_e=124 and t_{pre}=1.5 [s] are applied

3.3.4 Sensitivity analysis on memory time and prediction time length

The next sensitivity analysis examines the effect of memory time in PSWF-based ACFs and prediction time length on the prediction accuracy. Figs. 15, 16 and 17 show the comparisons of ρ on each case while changing N_e and t_{pre} values. α=0.01 is employed on *Cases* A and C, while α=0.2 is employed on *Case* B. Overall, the PSWF-based ACFs provide better prediction accuracies than the sample ACF based results, in particular the improvement in R^2 values is noteworthy. This fact indicates that the removal of large-lag time errors in sample ACF leads to improvement of the prediction accuracy. Notable improvements can be seen up to t_{pre}=3.0 [s], whereas when t_{pre}=6.0 [s], the overall performance by PSWF-based ACFs is almost comparable to the sample ACF based results.

If the value of N_e is too small, e.g. N_e=84 on *Cases* A and B or N_e=200 on *Case* C, the degree of improvement in the prediction accuracy is small. This implies that choosing too short memory time can result in deterioration of the prediction accuracy. Sufficient improvements in prediction accuracy can be achieved for N_e values of 124 (*Cases* A and B) or 250 (*Case* C) or more. Referring to Fig. 10, these N_e values correspond to the memory time of about 9 [s] for *Case* A and about 13 [s] for *Cases* B and C.

By Comparing *Cases* B and C results, which are those with the same T length, one can find that *Case* C has a higher prediction accuracy. This is owning to the smaller noise level α in *Case* C. It is inferred that under the same time length T, the larger Slepian frequency c value allows the choice of a smaller α and thus guarantees a stable prediction accuracy.

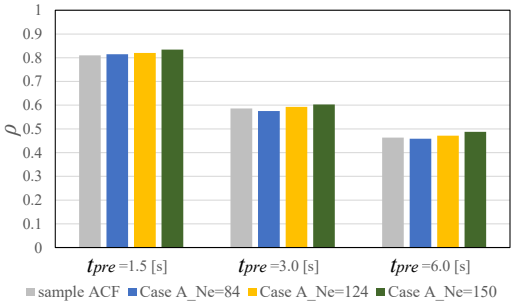

Fig. 15 Correlation coefficient ρ with respect to prediction time length t_{pre} and N_e values on *Case* A. α=0.01 is employed

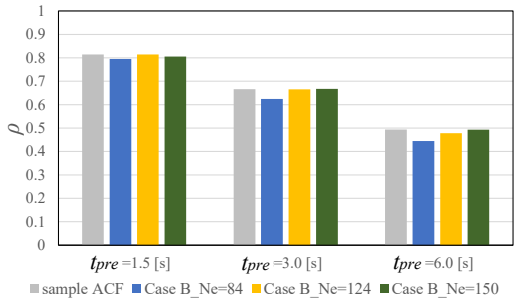

Fig. 16 Correlation coefficient ρ with respect to prediction time length t_{pre} and N_e values on *Case* B. α=0.01 is employed

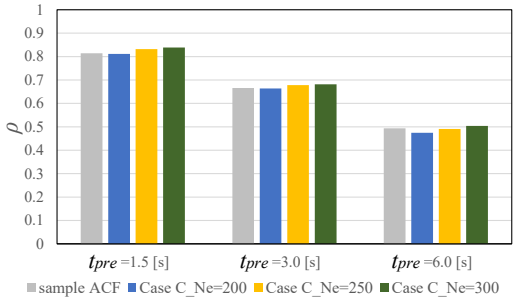

Fig. 17 Correlation coefficient ρ with respect to prediction time length t_{pre} and N_e values on *Case* C. α=0.01 is employed

4. APPLICATION TO FULL-SCALE MEASUREMENTS

4.1. Data Summary

In this section, full-scale measurements of ship motions of a large containership in size of 14,000TEU (Okada et al., 2017) are used as input for a series of ACF based predictions. As examples, two sets of 3600 [s] measurements of wave-induced vertical acceleration and roll motion at the Bosun store in the ship at different measurement periods are used, named as *State* 1 and *State* 2. The detailed locations of the ship on these states can be seen in Fig. A6 in Appendix 2 based on the GPS data histories. Associated integral wave parameters, representing the wave conditions during the measurement periods, have been provided by JWA, and Table 2 lists estimates of significant wave height, significant wave period, and mean wave direction, of which definitions follow e.g. (Goda, 2010). The parameters have been derived from a hindcast analysis made by NCEP and are the result of computations made using the third generation spectral wave model WAM (Komen et al., 1994).

The course and speed over ground during the measurements are examined based on the GPS data and plotted together with vertical acceleration and roll motion time series in Fig. 18. Time series data of the ship motions are stored at 10Hz using a gyro sensor. The vertical acceleration time series indicate stable mean values close the gravity acceleration (-9.81 [rad/s]), throughout the measurement time. The course is positive in the clockwise direction where North is 0 [deg]. As for *State* 1, the ship was sailing in the same direction with almost constant forward speed. Thus, it is deduced that only the non-stationarity in the seaway may influence the wave-induced responses in *State* 1. Since the mean wave direction over ground was 5.5 [deg] as seen from Table 2, it is assumed that the ship was sailing under nearly the following sea condition. On the other hand, *State* 2 indicates the large variations in course and ship speed. Such kind of maneuvering is expected to induce non-stationary effects in the wave-induced responses in *State* 2 on top of the non-stationarity in waves. One can find a significant difference in the amplitudes of vertical accelerations between *State* 1 and *State* 2, even though the significant wave height and wave period are similar in the two situations. This fact confirms that changes in ship speed and voyage direction has a significant effect on the motion amplitude. For *State* 1, a large roll motion has been observed, while the roll motion under *State* 2 is not significant, although large variations in the mean value occurs over a long period of time.

The PSDs of vertical accelerations are shown in Fig. 19, together with zooms of high frequency components. The gravity acceleration has been subtracted from each signal of vertical acceleration in calculating PSDs. Although the PSDs are noisy because of the limited time range and of spectral leakage (Box et al., 2008), the PSDs are wide-banded in frequency content especially in *State* 1. The high frequency components distribute within 3.0 to 9.0Hz. As a reference, Fig. 20 shows a zoom of the times series at 1000-1100 [s] under *State* 1. The mean values are adjusted to zero in Fig. 20. The high frequency noise caused by structural vibrations appears significant in the raw vertical acceleration time series. This high frequency

noise has been removed from the measurements in order to distinguish the wave-induced components. Hence, the LPF with cutoff frequency of 1.0[rad/s] is applied to the raw data and are compared in the figure. As seen from Fig. 20, the high frequency components can be removed from the vertical acceleration measurements by the LPF. In the following prediction cases, the low-pass filtered data with cutoff frequency of 1.0 [rad/s] are used for a series of predictions, both for *State* 1 and *State* 2. Fig. 21 shows the CDFs of the vertical acceleration measurements under *State* 1 and *State* 2. From the CDFs, the measurements under *State* 1 are almost in stationary state, whereas non-stationarities can be found in *State* 2 measurements.

The PSDs of roll motion measurements are shown in Fig. 22. The PSD under *State* 1 indicates a quite narrow-banded response with large amplitudes, while *State* 2 indicates small amplitudes. It is deduced that parametric rolling likely led to the large roll motion amplitudes in *State* 1, as the ship sailed in following sea in this condition. In this sense, conditions are equivalent to cases studied by (Nielsen and Jensen, 2009) which showed that encounters of parametric rolling may appear quite regularly when conditions are right; almost like large rolling is being turned on and off with a fixed time interval. In contrast to *State* 1, speed and course controlling during *State* 2 voyage suppressed large motion. The results and discussion onwards will focus only on the vertical accelerations, while those on the roll motions are presented in Appendix 3; noting that roll motion generally is a more resonant type of response (narrow-banded in its frequency content) hence being relatively easier to deterministically predict.

Table 2 Sea states estimated by JWA. Note that mean wave direction is defined in the standard NED frame of reference and indicates where the waves come from.

	Significant wave height	Significant wave period	Mean wave direction
State 1	5.05 [m]	8.3 [s]	5.5 [deg]
State 2	4.17 [m]	7.2 [s]	197.3 [deg]

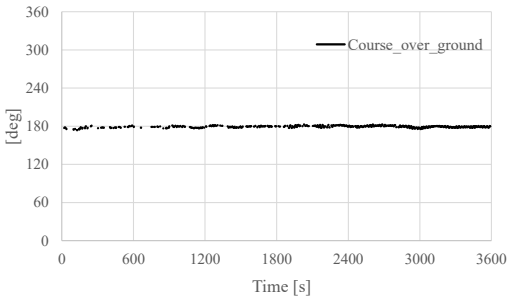

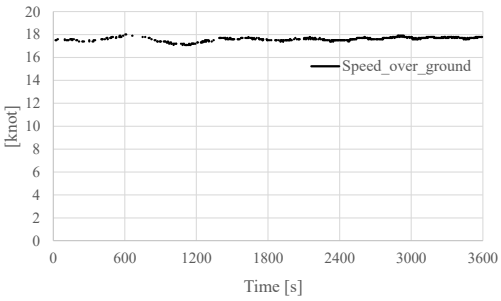

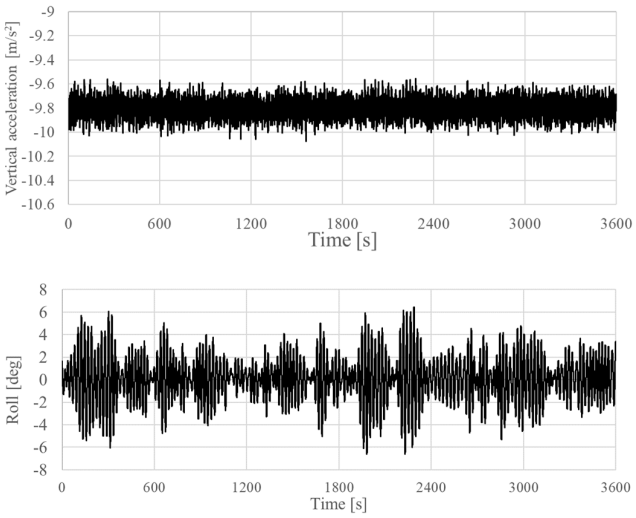

a) *State* 1

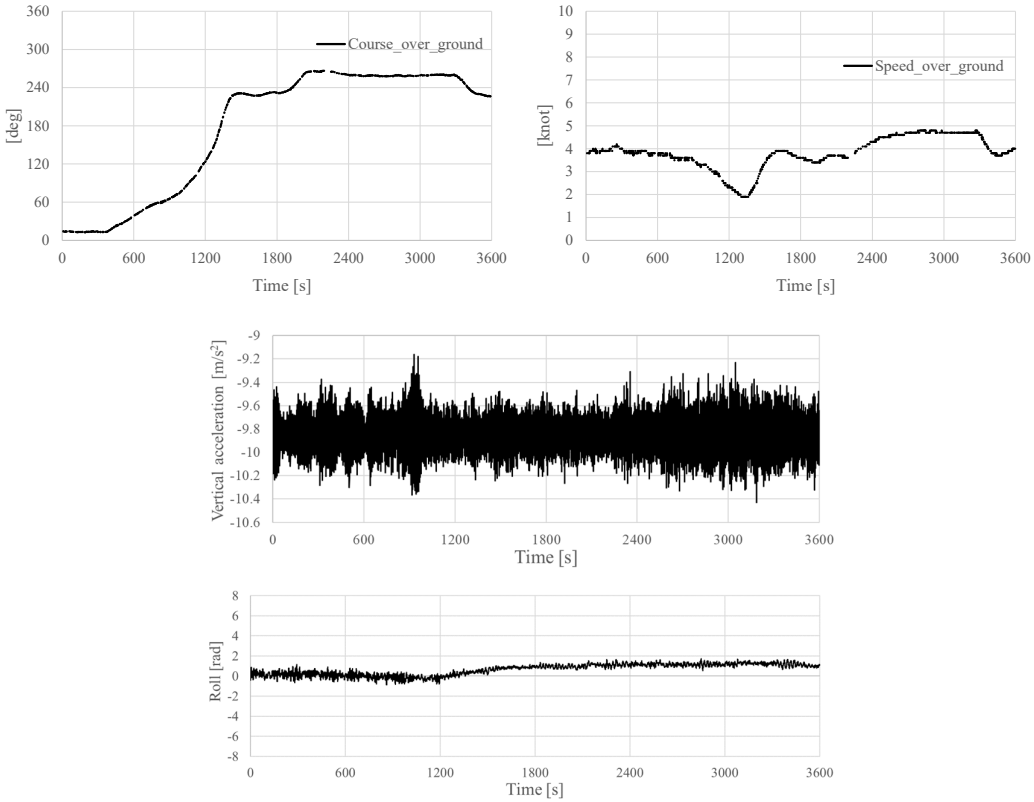

b) *State* 2

Fig. 18 Course, ship speed, vertical acceleration, and roll motion histories during the measurements on *State* 1 and *State* 2

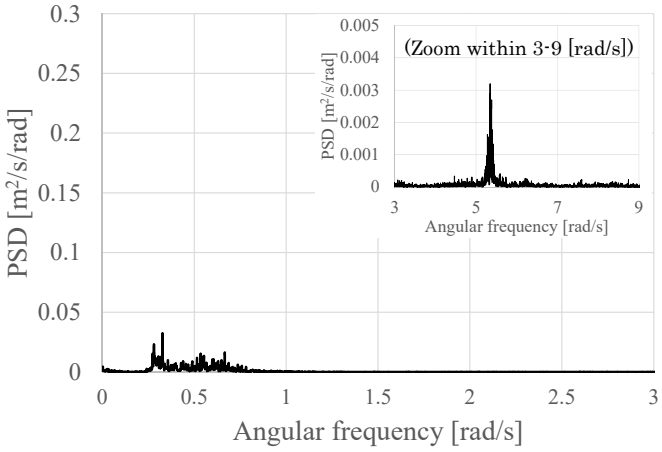

a) *State* 1

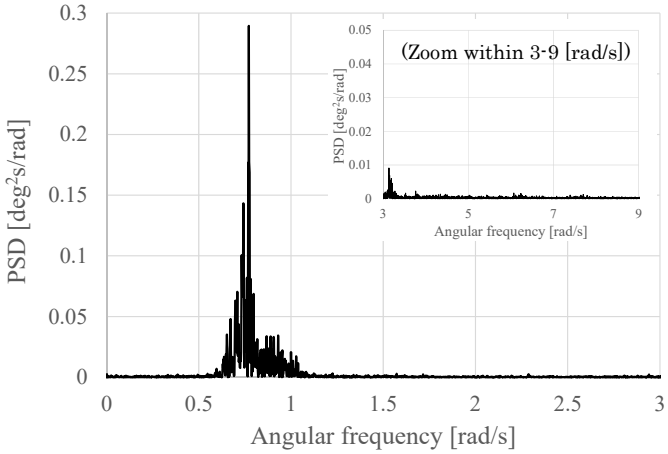

b) *State* 2

Fig. 19 PSDs of vertical acceleration under *State* 1 and *State* 2

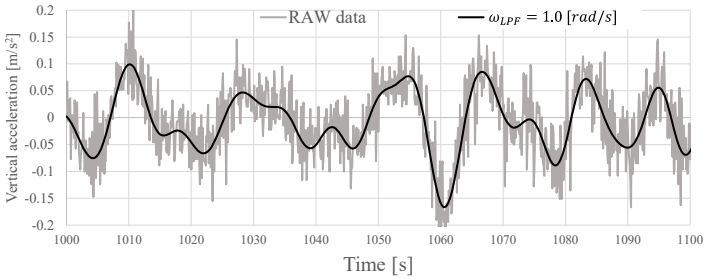

Fig. 20 Zoom of times series of vertical acceleration within 1000-1100 [s] under *State* 1 comparing with low-pass filtered one

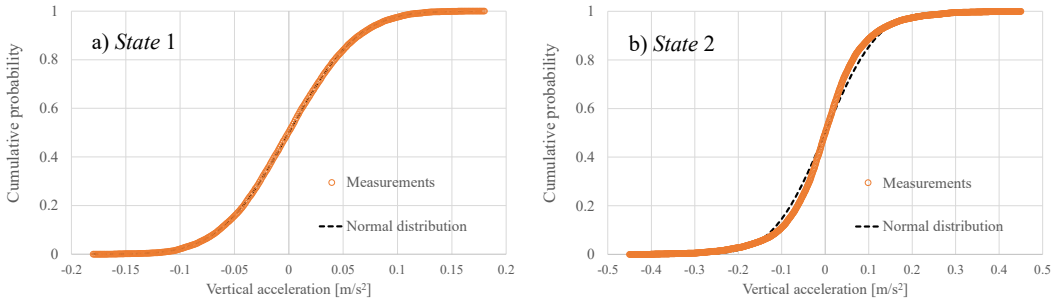

Fig. 21 Cumulative probability distributions of the vertical acceleration of the full scale containership under *State* 1 and *State* 2

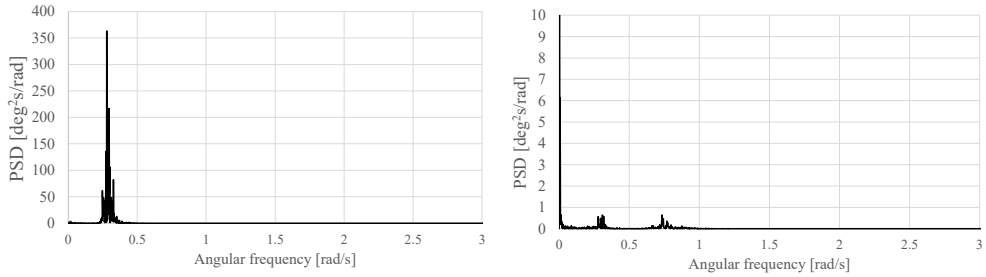

a) *State* 1 b) *State* 2

Fig. 22 PSDs of roll motion under *State* and *State* 2

4.2. PSWF Settings for Instantaneous ACFs

The predictions are made using the recent 100 [s] past measurements and instantaneous ACFs with same length in every case, i.e. the AC matrix size of n=1001 as sampling frequency of 10Hz. The PSWF of c=300 is used. According to the relationship in Eq. (6), T=100 [s] and Ω=3 [rad/s] are employed. Using a typical ACF from the vertical acceleration measurements under *State* 1, the non-dimensional variance values in PSWF-based ACFs, i.e. $r_p(0)/r_s(0)$, and the memory time of PSWF-based ACFs are calculated and plotted with respect to N_e values in Fig. 23. The memory time in Fig. 23 b) is defined as the time over which the ACF converged to 0.1% of the signal variance or less, i.e. $0.001r_s(0)$. From Fig. 23 a), the appropriate representations of $r_s(0)$ value by PSWF is expected when N_e>50. In the following prediction cases, three N_e values, N_e=84, 124 and 150 with expected memory time as 76 [s], 88 [s], and 94 [s], respectively, are adopted and compared in the results.

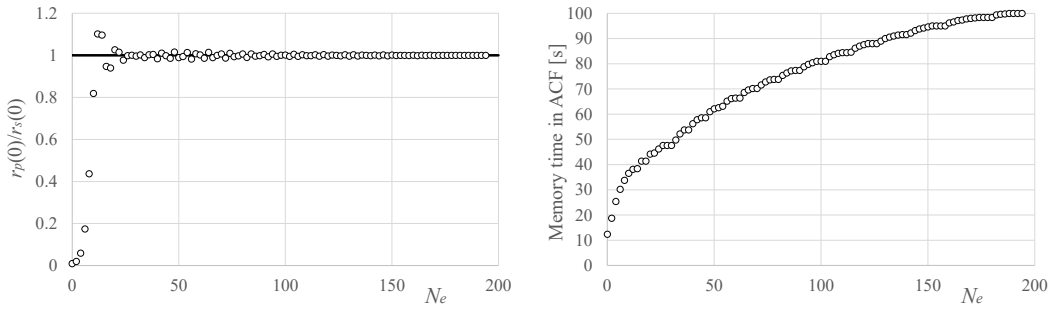

a) ACF at t=0 [s] b) Memory time of ACF

Fig. 23 Plots of $r_p(0)/r_s(0)$ with respect to N_e values (left) and memory time of PSWF-based ACFs with respect to N_e values (right)

4.3. Prediction Results Using Instantaneous ACFs

A sequence of predictions of the vertical acceleration is made according to the procedure given by Fig. 5. Three t_{pre} values, t_{pre}=10, 30, and 60 [s], are adopted, using the sample ACF and PSWF-based ACFs with AC matrix modification. The metric, ρ, is again used for evaluating the accuracy, while taking the N value in Eq. (16) as the number of predictions or measurements corresponding to the time range of from T [s] to 3600 [s]. α=0.2 is used for setting the noise level by Eq. (10). Figs. 24 and 25 show the comparisons of ρ on the vertical acceleration under *State* 1 and *State* 2. All in all, it can be again found that PSWF improves the accuracy of the sample ACF, and the following yields details of the evaluation.

The improvement is rather notable for t_{pre}=10 [s], which implies that the PSWF-based ACFs are more effective in improving the accuracy of the most recent predictions. The same is true in the cases with t_{pre}=30 [s]. For the cases t_{pre}=60 [s], the prediction accuracy by PSWF-based ACF is almost comparable to the sample ACF, however, the resulting ρ and R^2 values are low in most cases. It is deduced that for securing prediction accuracy on such long prediction time ahead, the ACF should be taken from longer time period(s). This point can be examined from a series of comparisons with the prediction results from longer periods, i.e. larger T values, see Section 4.4. The prediction accuracy by PSWF-based ACFs depends on the value of N_e. However, in the present demonstrations, focus will not be on selecting the optimal N_e. For practical application, a selection method could be for instance be developed by noting that the N_e value should be taken large enough to accurately represent the signal variance, $r_s(0)$, cf. Fig. 23 a); but, as mentioned, this task is not studied further in this study.

The prediction results of the vertical acceleration under *State* 2 within 900-1000 [s] from the sample ACFs and PSWF-based ACFs (N_e=124) are compared in Fig. 26. The acceleration of gravity (= 9.81 [m/s^2]) is subtracted from the measurements and predictions. Here t_{pre}=10 [s] has been adopted. In Fig. 26, abrupt changes in predictions denote the update of start time of a prediction, cf. Fig. 5. Within 900-1000 [s], large amplitudes in the vertical acceleration have been observed, see Fig. 18 b). From the figure, it can be seen that the PSWF-based ACFs predict the motion amplitudes with reasonable accuracy, whereas the sample

ACF underestimates the amplitudes.

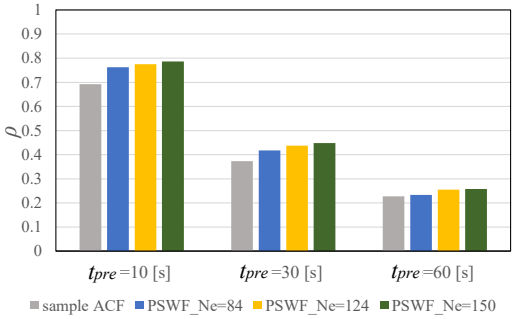

Fig. 24 Comparisons of ρ values of prediction results on vertical acceleration under *State* 1. Instantaneous ACFs are taken from recent 100 [sec]. α=0.2 is employed

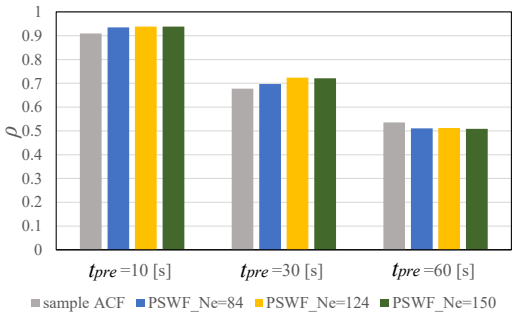

Fig. 25 Comparisons of ρ values of prediction results on vertical acceleration under *State* 2. Instantaneous ACFs are taken from recent 100 [sec]. α=0.2 is employed

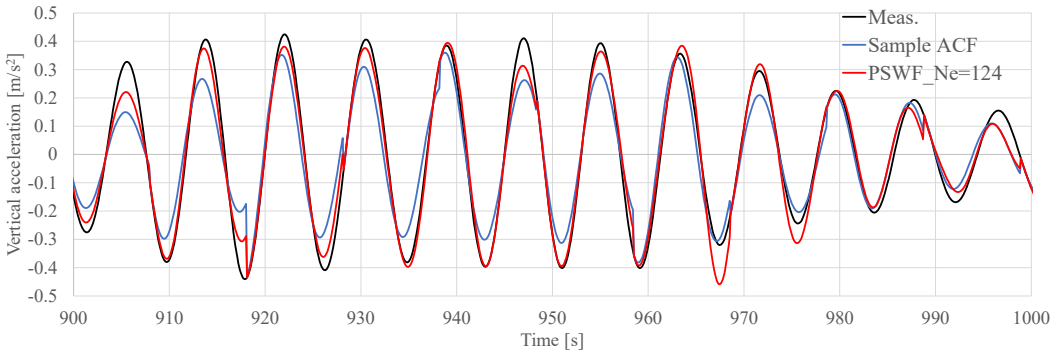

Fig. 26 Comparisons of prediction results within 900-1000 [s] from sample ACF and PSWF-based ACF (N_e=124, α=0.2) on vertical acceleration under *State* 2. t_{pre}=10 [s] is used. Instantaneous ACFs are taken from recent 100 [sec].

4.4. Instantaneous ACF vs. Long-term ACF

Finally, the presented prediction results based on the instantaneous ACFs are compared with those when the sample ACFs are taken from recent measurements but of a long(er) period; in the following referring to this ACF as 'long-term ACF'. The long-term ACFs are calculated from the past 3600 [s] before starting a prediction, i.e. T=3600 [s], and then the predictions are made using past 100 [s] measurements using ACF up to 100 [s], i.e. the AC matrix size is n=1001. Based on the course and speed records, investigation of the former 3600 [s] before *State* 1 and before *State* 2 confirms that the ship was sailing at almost constant course and speed in both cases.

The predictions on vertical accelerations under *State* 1 and *State* 2 are made in the same manner as instantaneous ACF cases according the procedure in Fig. 5. The evaluation metric ρ are shown in Figs. 27 and 28 that contain the comparison with the instantaneous ACF-based results. Note that the sample ACFs are directly used for predictions based on the long-term ACFs. N_e=124 and α=0.2 are used as with the instantaneous ACF-based results using PSWFs. Sort of intermediate ρ values are also calculated, thus the metrics are computed for the first and second halves of the full time span, i.e. a computation for the 100-2000 [s] span and another for the 2000-3600[s] span on both *State* 1 and *State* 2; these results are shown in subfigures b) and c). From Fig. 27, in the case of *State* 1, the long-term ACFs give the best accuracy, at the expense of computational efforts in calculating sample ACFs of recent 3600[s]. Better accuracies are also found for the cases with a long prediction time t_{pre}. As can be found from the probability distribution in *State* 1, see Fig. 21, the vertical acceleration under *State* 1 can be regarded as very close to being stationary, and, consequently, the larger value of T is considered to guarantee better prediction accuracy.

However, in the case of *State* 2, see Fig. 28, the long-term ACF does not provide better accuracies than the instantaneous ACF based results, in particular in the 2000-3600 [s] span, as evaluated by ρ. This trend becomes remarkable for longer t_{pre} cases, see t_{pre}=30 [s] and 60 [s] results. It is clear from Fig. 18 b) that the ship course was changed during *State* 2, and this has in turn led to a significant change in the heading angle relative to the waves. Thus, it is inferred that such maneuvering-induced non-stationarity results in the deterioration of the predictions using the long-term ACFs. It is also evident from Fig. 28 that the use of the instantaneous ACFs is effective in predicting wave-induced responses where maneuvering effects occur.

As presented by (Nielsen et al., 2018), the instantaneous ACFs and corresponding AC matrices can be stored for a certain period and reused for predictions, an approach by which the computational efforts of calculating the instantaneous ACF and AC matrix inversions can be reduced. For this reason, the instantaneous ACFs are updated every 300 or 600 [s], i.e., only executing *Steps* 1 to 3 in Fig. 5 every 300 or 600 [s]. In this case, the prediction results of the vertical acceleration under *State* 2 are compared in Fig. 29. t_{pre}=30 [s] is adopted and the sample ACFs are used for all predictions without using PSWF. For comparison, the instantaneous ACF based results from every 30 [s] updates of instantaneous ACFs, which are already shown in Fig. 28, are plotted. From Fig. 29 a) and Fig. 29 b), the prediction accuracies are almost comparable within 100-3600 [s] or 2000-3600 [s], however, the accuracy has deteriorated within

100-2000 [s] when the 300 or 600 [s] updates are applied. In consequence of these demonstrations, it is inferred that frequent updates of instantaneous ACFs may be ideal, in particular if the ship response includes maneuvering-induced non-stationary effects.

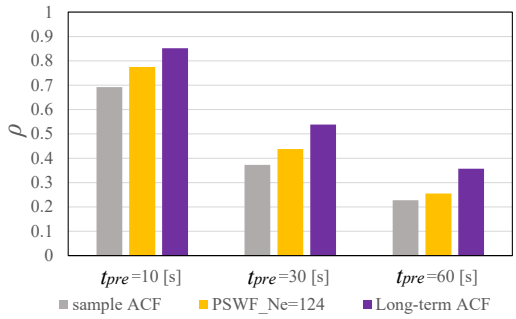

a) 100-3600 [s]

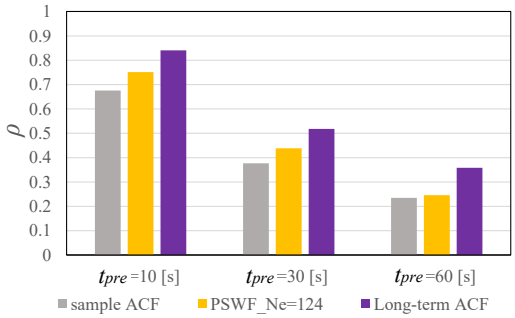

b) 100-2000 [s]

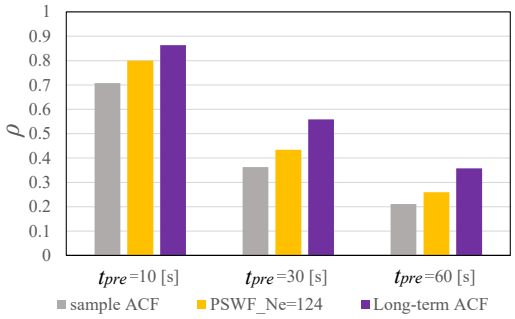

c) 2000-3600 [s]

Fig. 27 Comparisons of ρ values of prediction results on vertical acceleration under *State* 1. Compared with long-term ACF based results. α=0.2 is employed for PSWF-based predictions

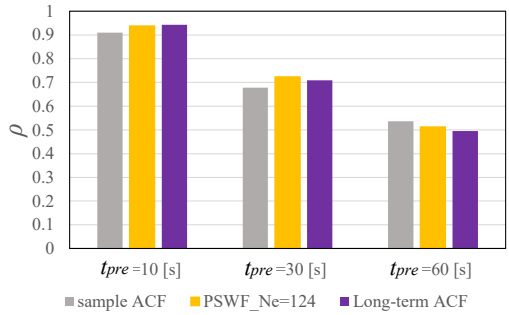

a) 100-3600 [s]

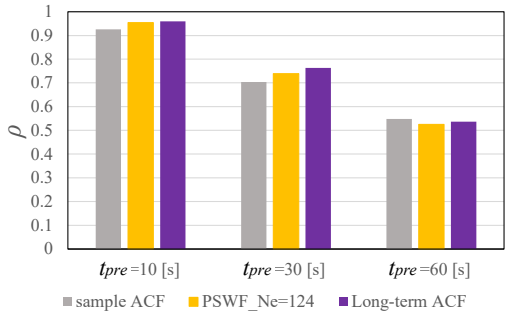

b) 100-2000 [s]

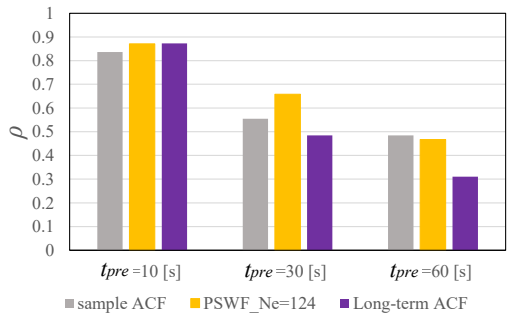

c) 2000-3600 [s]

Fig. 28 Comparisons of ρ values of prediction results on vertical acceleration under *State* 2. Compared with long-term ACF based results. α=0.2 is employed for PSWF-based predictions

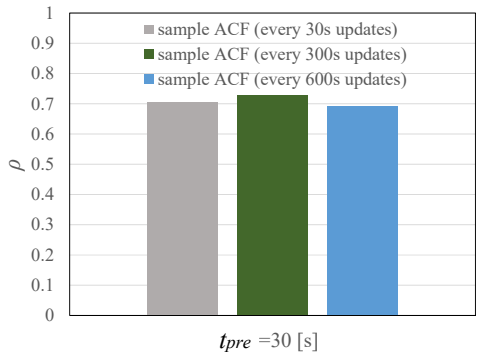

a) 100-3600 [s]

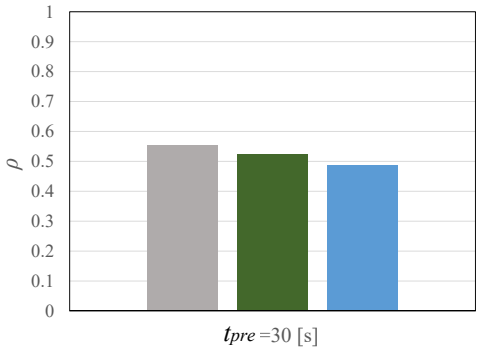

b) 100-2000 [s]

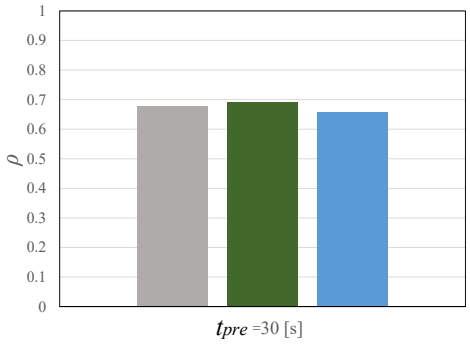

c) 2000-3600 [s]

Fig. 29 Comparisons of ρ values of prediction results on vertical acceleration under *State* 2. Compared with long-term ACF based results

5. CONCLUSIONS

This paper studied real-time deterministic prediction of wave-induced ship motions using the autocorrelation functions (ACFs) from short-time measurements, namely the instantaneous ACFs. The

Prolate Spheroidal Wave Functions (PSWF) were introduced to smooth the sample ACF, together with a modification of the autocorrelation (AC) matrix, in order to ensure positive definiteness. The validity of PSWF-based ACFs is checked using stationary and non-stationary ship motion measurements from, respectively, model experiments under stationary wave excitations and in-service operations of a container ship. The following conclusions can be drawn:

1. By modifying the PSWF-based power spectrum density (PSD) in terms of removal of negative PSD together with noise inclusion, positive definiteness of AC matrices can be ensured. This procedure facilitates the computation of ACF-based predictions in real-time without the need to compute eigenvalues in AC matrices.
2. A series of validations using experimentally measured heave motion revealed that the use of PSWF-based ACFs led to better prediction accuracy than direct use of sample ACFs, owing to the smoothing of large-lag time errors in the sample ACFs. The application of smallest possible noise level was found to be ideal for obtaining better prediction results. The larger Slepian frequency value allows the choice of the smaller noise level and then guarantees a stable prediction accuracy.
3. Improvement of prediction accuracy by PSWF-based ACFs was also found for cases based on full-scale ship motions, where the vertical acceleration of the ship was considered. In the demonstrations, the better prediction accuracy was confirmed by comparing to similar results based on the sample ACF; this was observed for prediction horizons up to 30 [s]. It was also shown that the PSWF-based ACFs predict the extreme motion amplitudes with reasonable accuracy, whereas the sample ACF underestimates the amplitudes.
4. When the vertical acceleration measurements are from a stationary state with only insignificant maneuvering effects, the ACFs from recent long-time measurements (long-term ACFs) provided better prediction accuracy. On the other hand, when the vertical acceleration measurements are influenced by maneuvering effects, a benefit of using the instantaneous ACFs was demonstrated by comparing with long-term ACF based results. In this sense, the effectiveness of using the instantaneous ACF on non-stationary wave-induced responses has been presented, and it was inferred that (large) changes in ship speed and heading angle relative to waves require frequent updates of the instantaneous ACFs.

The present ACF-based prediction method has a potential to be useful for extrapolating Karhunen–Loeve representation of ocean waves (Sclavounos, 2012); noting that the Karhunen–Loeve wave representation generally can be applied for efficient extreme value predictions together with the First Order Reliability Method (Jensen, 2021; Takami et al., 2020a). This is currently under investigation.

ACKNOWLEDGEMENTS

The authors are grateful to Assoc. prof. Astrid H. Brodtkorb for providing experimental data used in this paper. The full-scale measurements were made as part of the *i-Shipping* (operation) Project supported by

Ministry of Land, Infrastructure and Transport in Japan. The authors would like to acknowledge Monohakobi Technology Institute Co., Ltd for providing the full-scale measurements data. The authors also acknowledge all members of Structural Strength Evaluation Dept. in National Maritime Research Institute for thorough discussion.

REFERENCES

Andersen, I.M.V., Jensen, J.J., Nielsen, U.D., 2013. Evaluation of Response Prediction Procedures using Full Scale Measurements for a Container Ship, in: Proceedings of PRADS2013. Copenhagen, pp. 793–800.

Box, G.E.P., Jenkins, G.M., Reinsel, G.C., 2008. Time Series Analysis: Forecasting and Control, 4th ed. Wiley.

Brodtkorb, P.A., Johannesson, P., Lindgren, G., Rychlik, I., Ryden, J., Sjo, E., 2000. WAFO - A Matlab toolbox for analysis of random waves and loads. Tutor. WAFO version 2017.

Duan, S., Ma, Q., Huang, L., Ma, X., 2019. A LSTM Deep Learning Model for Deterministic Ship Motions Estimation Using Wave-Excitation Inputs, in: Proceedings of the Twenty-Ninth (2019) International Ocean and Polar Engineering Conference. Honolulu, Hawaii, pp. 959–965.

Duan, W.Y., Huang, L., Han, Y., Zhang, Y., Huang, S., 2015a. A hybrid AR-EMD-SVR model for the short-term prediction of nonlinear and non-stationary ship motion. J. Zhejiang Univ. A 16, 562–576.

Duan, W.Y., Huang, L.M., Han, Y., Wang, R., 2015b. IRF - AR model for short-term prediction of ship motion, in: Proceedings of the International Offshore and Polar Engineering Conference. Shanghai, pp. 59–66.

Goda, Y., 2010. Random Seas and Design of Maritime Structures, Advanced Series on Ocean Engineering: Volume 33, 3rd ed. World Scientific.

Gray, R.M., 2006. Toeplitz and Circulant Matrices: A review. Found. Trends Commun. Inf. Theory 2, 155–239.

Huang, L., Duan, W., Han, Y., Chen, Y.-S., 2014. A Review of Short-term Prediction Techniques for Ship Motions in Seaway. J. Sh. Mech. 18, 1534–1542.

Huang, L., Duan, W., Han, Y., Yu, D., Elhandad, A., 2015. Extending the Scope of AR Model in Forecasting Non-stationary Ship Motion by Using AR-EMD Technique. J. Sh. Mech. 19, 1033–1049.

Jensen, J.J., 2021. Use of Prolate Spheroidal Wave Functions in the Time Domain First Order Reliability Method, in: Proceedings of Practical Design of Ships and Other Floating Structures. PRADS 2019. Yokohama, pp. 760–769. https://doi.org/10.1007/978-981-15-4624-2_46

Jensen, J.J., 2001. Load and Global Response of Ships, Vol. 4 of Elsevier Ocean Engineering Book

Series, 1st ed. Elsevier.

Kitagawa, G., 2010. Introduction to Time Series Modeling, 1st ed. Chapman and Hall/CRC.

Komen, G.J., Cavaleri, L., Donelan, M., Hasselmann, K., Hasselmann, S., Janssen, P.A.E.M., 1994. Dynamics and modelling of ocean waves. Cambridge University Press.

Lindgren, G., 1970. Some properties of a normal process near a local maximum. Ann. Stat. 41, 1870–1883.

Ma, Y., Sclavounos, P.D., Cross-Whiter, J., Arora, D., 2018. Wave forecast and its application to the optimal control of offshore floating wind turbine for load mitigation. Renew. Energy 128, 163–176.

McLeod, A.I., Jimenez, C., 1984. Nonnegative Definiteness of the Sample Autocovariance Function. Am. Stat. 38, 297–298. https://doi.org/10.1080/00031305.1984.10483233

McMurry, T.L., Politis, D.N., 2015. High-dimensional autocovariance matrices and optimal linear prediction. Electron. J. Stat. 9, 753–788.

Moore, I.C., Cada, M., 2004. Prolate spheroidal wave functions, an introduction to the Slepian series and its properties. Appl. Comput. Harmon. Anal. 16, 208–230. https://doi.org/10.1016/j.acha.2004.03.004

Nakatani, T., Blanke, M., Galeazzi, R., 2006. Pitch Motion Stabilization by Propeller Speed Control Using Statistical Controller Design, in: Proceedings of the 7th IFAC Conf. on Manoeuvring and Control of Marine Craft. Lisbon.

Nielsen, U.D., Brodtkorb, A.H., Jensen, J.J., 2018. Response predictions using the observed autocorrelation function. Mar. Struct. 58, 31–52.

Nielsen, U.D., Jensen, J.J., 2017. Deterministic predictions of vessel responses based on past measurements, in: Proceedings of the International Offshore and Polar Engineering Conference. San Francisco, California, pp. 513–519.

Nielsen, U.D., Jensen, J.J., 2009. Numerical simulations of the rolling of a ship in a stochastic sea - Evaluations by use of MCS and FORM, in: Proceedings of the International Conference on Offshore Mechanics and Arctic Engineering - OMAE. Honolulu, Hawaii, pp. 523–533. https://doi.org/10.1115/OMAE2009-79765

Okada, T., Kawamura, Y., Kato, J., Ando, H., Yonezawa, T., Kimura, F., Toyoda, M., Yamanouchi, A., Arima, T., Oka, M., Matsumoto, T., Kakizaki, H., 2017. Outline of the research project on hull structure health monitoring of 14,000TEU large container ships (in Japanese), in: Conference Proceedings, the Japan Society of Naval Architects and Ocean Engineers, 24. Tokyo, pp. 31–35.

Peña-Sanchez, Y., Mérigaud, A., Ringwood, J. V, 2020. Short-Term Forecasting of Sea Surface Elevation for Wave Energy Applications: The Autoregressive Model Revisited. IEEE J. Ocean. Eng. 45, 462–471.

Perez, T., 2005. Ship Motion Control; Course Keeping and Roll Stabilisation Using Rudder and Fins. Springer.

Sclavounos, P.D., 2012. Karhunen-Loeve representation of stochastic ocean waves. Proc. R. Soc. A Math. Phys. Eng. Sci. 468, 2574–2594. https://doi.org/10.1098/rspa.2012.0063

Sclavounos, P.D., Ma, Y., 2018. Artificial intelligence machine learning in marine hydrodynamics, in: Proceedings of the International Conference on Offshore Mechanics and Arctic Engineering - OMAE. Madrid. https://doi.org/10.1115/OMAE2018-77599

Slepian, D., Pollak, H.O., 1961. Prolate spheroidal wave functions, fourier analysis and uncertainty - I. Bell Syst. Tech. J. 40, 43–63.

Takami, T., Iijima, K., Jensen, J.J., 2020a. Extreme value prediction of nonlinear ship loads by FORM using Prolate Spheroidal Wave Functions. Mar. Struct. 72, 102760. https://doi.org/10.1016/j.marstruc.2020.102760

Takami, T., Nielsen, U.D., Jensen, J.J., 2020b. Estimation of Autocorrelation Function and Spectrum Density of Wave-induced Responses Using Prolate Spheroidal Wave Functions (accepted for publication). J. Mar. Sci. Technol.

Takami, T., Nielsen, U.D., Jensen, J.J., 2020c. Deterministic Prediction of Wave-induced Ship Responses Based on Corrected Autocorrelation Functions, in: Conference Proceedings of The Japan Society of Naval Architects and Ocean Engineering,Vol.31. Online.

Taylor, R., 1990. Interpretation of the Correlation Coefficient: A Basic Review. J. Diagnostic Med. Sonogr. 6, 35–39.

Xiao, H., Rokhlin, V., Yarvin, N., 2001. Prolate spheroidal wavefunctions, quadrature and interpolation. Inverse Probl. 17, 805–838.

Zhang, G., Tan, F., Wu, Y., 2020. Ship Motion Attitude Prediction Based on an Adaptive Dynamic Particle Swarm Optimization Algorithm and Bidirectional LSTM Neural Network (May 2020). IEEE Access 8, 90087–90098. https://doi.org/10.1109/ACCESS.2020.2993909

APPENDIX 1

The Determination Coefficient R^2 can calculated according to

$$R^2 = 1 - \frac{\sum_{i=1}^{N}(\hat{x}_i - x_i)^2}{\sum_{i=1}^{N}(x_i - \mu_x)^2} \tag{A1}$$

R^2 values with respect to prediction results are calculated in the same manner as the Pearson Correlation Coefficient ρ for experimental measurements and full-scale vertical acceleration measurements and are shown in Figs. A1 to A5. The same trends as those shown by the value of ρ is observed In terms of prediction accuracy.

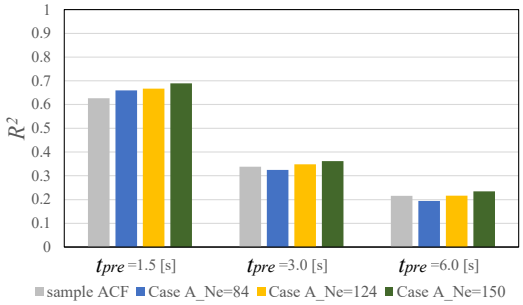

Fig. A1 Determination coefficient R^2 with respect to prediction time length t_{pre} and N_e values on *Case* A using experimental measurements. α=0.01 is employed

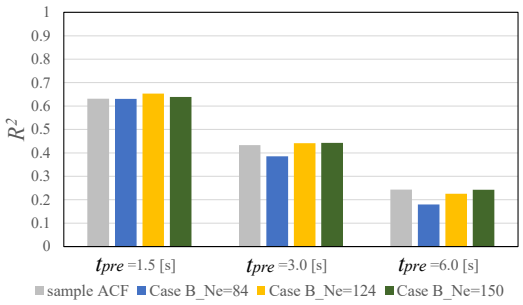

Fig. A2 Determination coefficient R^2 with respect to prediction time length t_{pre} and N_e values on *Case* B using experimental measurements. α=0.01 is employed

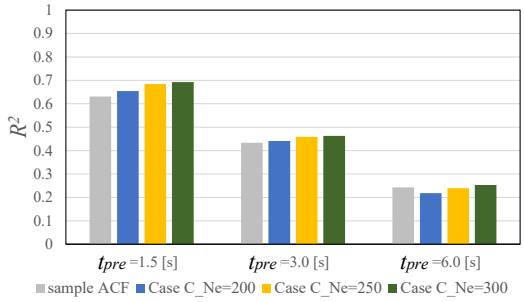

Fig. A3 Determination coefficient R^2 with respect to prediction time length t_{pre} and N_e values on *Case* C using experimental measurements. α=0.01 is employed

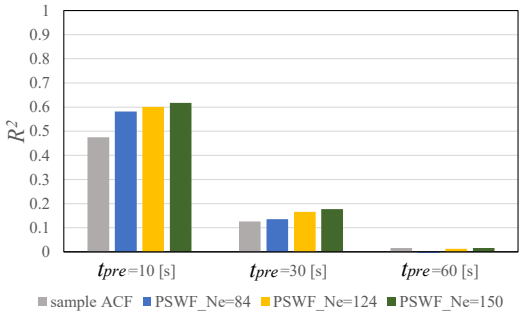

Fig. A4 Comparisons of R^2 of prediction results on vertical acceleration from full-scale measurements under *State* 1. Instantaneous ACFs are taken from recent 100 [sec]. α=0.2 is employed

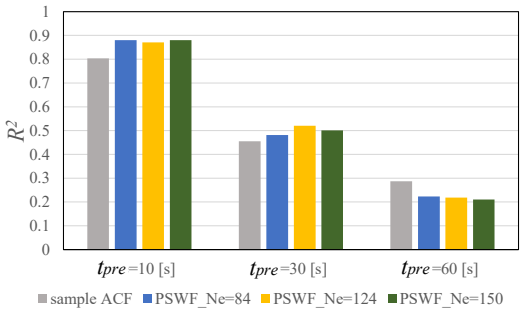

Fig. A5 Comparisons of R^2 of prediction results on vertical acceleration from full-scale measurements under *State* 2. Instantaneous ACFs are taken from recent 100 [sec]. α=0.2 is employed

APPENDIX 2

The voyage histories of the full scale container ship under *State* 1 and *State* 2 are examined by using the GPS data. The ship locations have been recorded at every 1 hour and plotted in Fig. A6. The positions of the ship for several hours before and after *State* 1 and *State* 2 are also plotted so that the sea routes can be visualized. It is presumed that the ship was changing the course from northward to westward direction, during *State* 2.

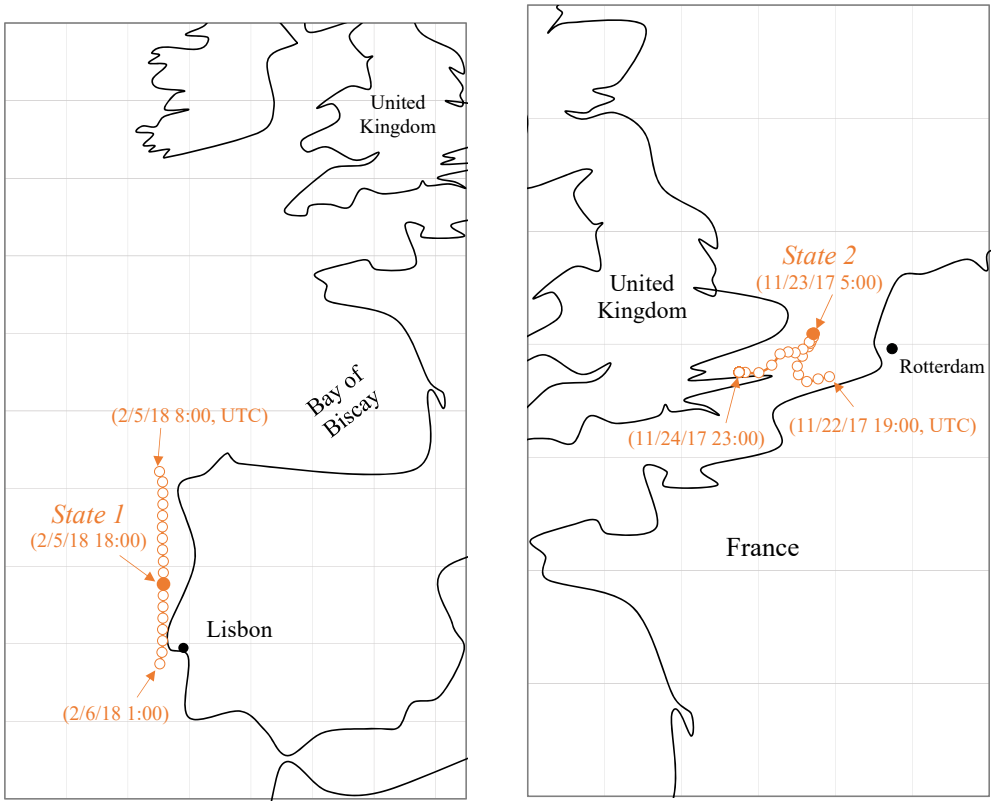

Fig. A6 Voyage histories of the full scale container ship derived from GPS data. Date and time are described in UTC

APPENDIX 3

The instantaneous ACF-based predictions on roll motion measurements are made in the same manner as the vertical acceleration cases in Section 4.3. The raw time series without application of the LPF are used for predictions. α=1.0 is employed for setting the noise level. The prediction results are compared in Figs. A7 and A8. For *State* 1, the tendency in terms of the improvement by the PSWF is in line with the vertical acceleration cases as described in Section 4.3. On the other hand, the changes in ρ and R^2 depending on t_{pre} are not significant in the case of *State* 2. This is due to a fact that the roll motion in this case indicates an extremely narrow-banded behaviour, i.e. the roll motion is dominated by the effects of resonance. This can be also found by looking the PSD shape of this case, see Fig. 22.

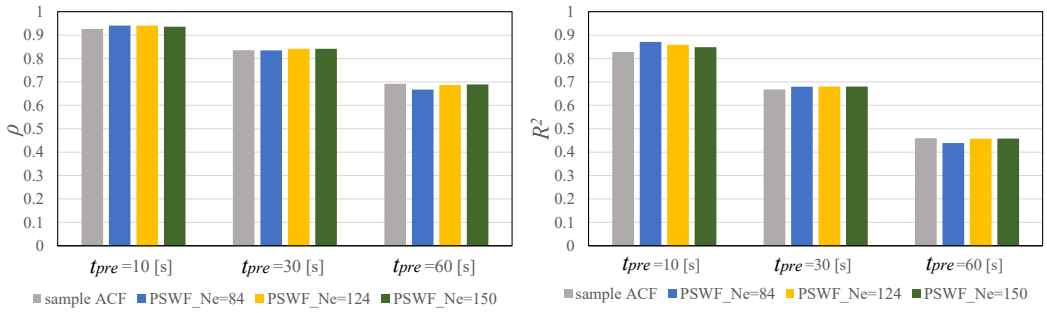

Fig. A7 Comparisons of ρ and R^2 of prediction results on roll motion under *State* 1. Instantaneous ACFs are taken from recent 100 [sec]. α=1.0 is employed

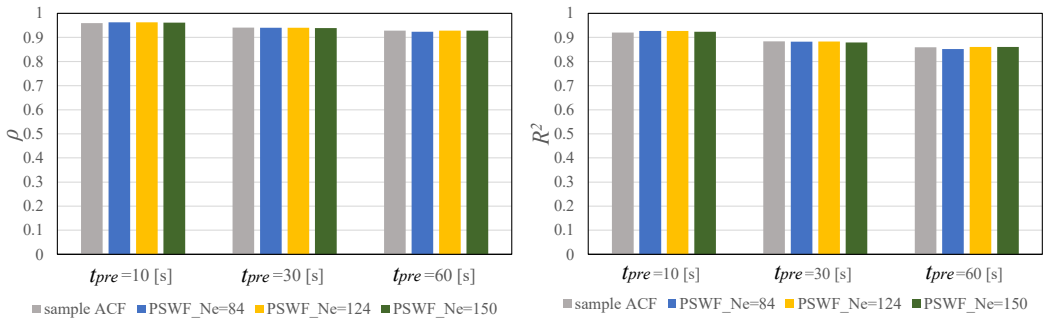

Fig. A8 Comparisons of ρ and R^2 of prediction results on roll motion under *State* 2. Instantaneous ACFs are taken from recent 100 [sec]. α=1.0 is employed